

Light scattering by a thin wire with a surface-plasmon resonance: Bifurcations of the Poynting vector field

B. S. Luk'yanchuk^{1,*} and V. Ternovsky²

¹Data Storage Institute, Agency for Science, Technology and Research, DSI Building, 5 Engineering Drive 1, Singapore 117608, Republic of Singapore

²M. V. Lomonosov Moscow State University, Faculty of Computing Mathematics and Cybernetics, MSU, Vorobjovy Gory, Moscow, 119899, Russia

(Received 5 October 2005; revised manuscript received 9 January 2006; published 28 June 2006)

We analyze the energy flow during the scattering of a plane wave by a small homogeneous cylinder in the vicinity of surface-plasmon resonance, where $\epsilon' = \text{Re } \epsilon = -1$ (ϵ stands for permittivity). For the case of small dissipation, $\epsilon'' = \text{Im } \epsilon << 1$, this scattering can strongly deviate from the classical dipole approximation (Rayleigh scattering). In certain specified cases, the Rayleigh scattering is replaced with an anomalous light scattering regardless the wire smallness. The phenomenon is based on interplay of the usual dissipative and radiative damping, where the latter is related to inverse transformation of localized resonant plasmons into scattered light. The anomalous light scattering possesses a variety of unusual features, such as an inverse hierarchy of optical resonances and a complicated near-field structure, which may include optical vortexes, optical whirlpools, and other peculiarities in nanoscale area.

DOI: 10.1103/PhysRevB.73.235432

PACS number(s): 73.20.Mf, 41.20.Jb, 41.85.Ja, 42.25.Fx

I. INTRODUCTION

Since the time when Lord Rayleigh¹ studied the problem of light scattering by a cylinder for the first time, it was analyzed in detail in later investigations of Wait, Kerker, and other authors; see Ref. 2. This problem has an exact solution, which, in fact, is quite comparable to the classical Mie theory.^{3–6} The fields around the cylinder are generally investigated in terms of specific far-field quantities, such as absorption, scattering, and extinction cross sections, or its far-field scattering diagram. These far-field characteristics are sufficient to explain many effects in optical tomography, meteorology, and astrophysics, and some applications, e.g., with cylindrical lens.⁷ More detailed information follows from the analysis of *near-field effects* and investigation of the energy flux (Poynting vector). Although this problem also refers to the classical problem of electromagnetism, it is attracting attention even now; see, e.g., Refs. 8–10. With the development of nanotechnologies, this problem has become especially important lately due to the studies of light scattering by *thin cylinders, fibers, and nanowires*. It is important for various modern applications, e.g., field concentration for nanopatterning with nanowires,¹¹ plasmonic nanolithography,¹² and near-field optical microscopy;¹³ astigmatic optical tweezers,¹⁴ nonlinear optics in nanowires,¹⁵ etc.

In spite of the importance of the mentioned problems, up to now the description of light scattering by small objects still has been based on the concept introduced by Rayleigh, where the small scatterer is treated as an electric dipole (a point dipole for a sphere or a linear dipole for a wire). From this approximation, the well-known formulas for scattering cross sections follows (see, e.g., Ref. 4):

$$Q_{\text{sca}} = \frac{8}{3} \left| \frac{n^2 - 1}{n^2 + 2} \right|^2 q^4, \quad \text{for sphere}, \quad (1)$$

and

$$Q_{\text{sca}} = \frac{\pi^2}{4} \left| \frac{n^2 - 1}{n^2 + 1} \right|^2 q^3, \quad \text{for cylinder}. \quad (2)$$

Equations (1) and (2), according to Ref. 4, are written in normalized dimensionless units; to find dimension cross sections σ_{sca} , one should multiply Q_{sca} to geometrical cross section σ_{geom} . For a sphere $\sigma_{\text{geom}} = \pi a^2$, where a is the radius of the spherical particle. For a cylinder $\sigma_{\text{geom}} = 2aL$, where a is the radius of the wire and $L \gg a$ is the length of the cylinder. Value $q = 2\pi a n_m / \lambda$ presents the size parameter, λ is the light wavelength, and n_m is the refractive index of the media. Complex refractive index of the particle is given by n_p ; value $n = n_p/n_m$ presents the relative variation of refractive index, the relative dielectric permittivity is given by $\epsilon = \epsilon_p/\epsilon_m \equiv n_p^2/n_m^2$.

Equations (1) and (2) have resonant denominators, which diverge at $n^2 = -2$ (for sphere) and $n^2 = -1$ (for cylinder). The physical meaning of the divergence is well known. When the frequency of the dipole eigenmode (surface localized plasmon) equals the one for the incident light, one has the case of resonance. If the dissipation rate is zero the amplitude of the resonant mode should diverge. The conventional way to avoid the divergence is to include finite dissipation, thus, with $\text{Im } \epsilon \neq 0$ expressions (1) and (2) remain finite.

However, as it was shown in Ref. 16, in addition to the usual dissipation the problem in question must possess the “radiative” damping, existing even at zero dissipation rates. This radiative damping is related to *emission of electromagnetic waves* due to inverse transformation of localized plasmons into propagating electromagnetic radiation. Taking into account this effect, one should replace Eqs. (1) and (2) by other expressions, obtained from the exact Mie solution or a similar solution for a cylinder, which includes the radiative damping explicitly. Interference of this scattered wave with an incident wave produces a complex near-field pattern, which leads to complicated bifurcations of the energy flux around the particle. This pattern is different from the pattern,

produced by Rayleigh scattering.¹⁷ For the case of a sphere, this complicated pattern was analyzed recently in Refs. 18–20, but we did not find in literature analysis for the case of a thin wire. We should emphasize that the effects of anomalous scattering are too complicated to see in the far field for the majority of investigated metals, such as gold, silver, and platinum. However, they can be quite pronounced in the near field.

Thus, the purpose of this paper is to discuss the anomalous light scattering and the peculiarities of the energy flux around a thin wire with surface plasmon resonance. It will be shown that in the specified region of parameters a thin wire produces a complicated near-field pattern. It gives controllable changes of the near field structure with changes of the incident light frequency.

II. SCATTERING AMPLITUDES AND PLASMON RESONANCES

Following Ref. 6, we consider a nondissipative media and a nonmagnetic circular cylinder of radius a ; z is the cylinder axis. Thus, $\mu_m = \mu_p = 1$, $\epsilon_m = n_m^2$, where μ_m and μ_p are magnetic permeabilities, n_m stands for the refractive index of the media and we additionally consider $\text{Im } \epsilon_m = 0$. In principle, the absorbing media can also be treated employing the method suggested by Ruppini.¹⁰ The dielectric permittivity of the cylinder is given by $\epsilon_p = n_p^2$ where n_p stands for the complex refractive index. Considering fields $\mathbf{E}, \mathbf{H} \propto e^{-i\omega t}$, one should use the solution of the vector Helmholtz equation $\Delta \mathbf{E} + k^2 \mathbf{E} = 0$ (and a similar equation for magnetic field \mathbf{H}), which should satisfy the boundary conditions for continuity of tangential components of the field on the surface of the cylinder. Inside the cylinder $k^2 = k_p^2$ and outside the cylinder $k^2 = k_m^2$, where $k_{n,m} = 2\pi n_{n,m}/\lambda$. The desired solution can be expressed through the eigenfunctions of the scalar wave equation $\Delta \psi + k^2 \psi = 0$ in cylindrical polar coordinates $\{r, \varphi, z\}$

$$\psi_\ell(r, \varphi, z) = Z_\ell(\rho) e^{i\ell\varphi} e^{ihz}, \quad \rho = r\sqrt{k^2 - h^2}, \quad (3)$$

where h is the separation constant and $Z_\ell(\rho)$ is the appropriate Bessel function. For the internal region, one should use the Bessel function $J_\ell(\rho)$, and for the media around the cylinder, one should use the i function $H_\ell^{(1)}(\rho) = J_\ell(\rho) + iN_\ell(\rho)$ to satisfy the emission condition at infinity. It is well known that the surface plasmons are excited in the case of perpendicular polarization, $\mathbf{E} \perp z$ (TE mode) and are not excited with $\mathbf{E} \parallel z$ (TM mode). Thus, we will discuss the particular case of TE mode. Let us first consider the normal incidence of radiation. For this case, the separation constant h in (3) is zero and the incident, scattered, and transmitted fields are presented by simple formulas.⁶ Employing the linearity of the Maxwell equations, we normalize the vector of the incident electric field, $|\mathbf{E}^{(i)}| = 1$. Then the incident fields (indicated by index i) are given by

$$\begin{aligned} E_r^{(i)} &= \sin \varphi e^{-ik_m r} \cos \varphi, & E_\varphi^{(i)} &= \cos \varphi e^{-ik_m r} \cos \varphi, \\ H_z^{(i)} &= -e^{-ik_m r} \cos \varphi. \end{aligned} \quad (4)$$

The scattered fields (indicated by index s) are expanded in terms of Hankel functions

$$\begin{aligned} E_r^{(s)} &= -\frac{1}{k_m r} \sum_{\ell=-\infty}^{\infty} (-i)^\ell \ell a_\ell H_\ell^{(1)}(k_m r) e^{i\ell\varphi}, \\ E_\varphi^{(s)} &= -i \sum_{\ell=-\infty}^{\infty} (-i)^\ell a_\ell H_\ell^{(1)\prime}(k_m r) e^{i\ell\varphi}, \\ H_z^{(s)} &= \sum_{\ell=-\infty}^{\infty} (-i)^\ell a_\ell H_\ell^{(1)}(k_m r) e^{i\ell\varphi}. \end{aligned} \quad (5)$$

The transmitted fields inside the cylinder (indicated by index t) are written in the form

$$\begin{aligned} E_r^{(t)} &= \frac{1}{k_p r} \sum_{\ell=-\infty}^{\infty} (-i)^\ell \ell b_\ell J_\ell(k_p r) e^{i\ell\varphi}, \\ E_\varphi^{(t)} &= i \sum_{\ell=-\infty}^{\infty} (-i)^\ell b_\ell J_\ell'(k_p r) e^{i\ell\varphi}, \\ H_z^{(t)} &= -n_p \sum_{\ell=-\infty}^{\infty} (-i)^\ell b_\ell J_\ell(k_p r) e^{i\ell\varphi}. \end{aligned} \quad (6)$$

Prime denotes the derivative over the entire function's argument, i.e., $J'_\ell(z) \equiv dJ_\ell(z)/dz$, etc. The amplitudes a_ℓ and b_ℓ are defined according to the following expressions:

$$\begin{aligned} a_\ell &= \frac{n J_\ell(nq) J'_\ell(q) - J'_\ell(nq) J_\ell(q)}{n J_\ell(nq) H_\ell^{(1)\prime}(q) - J'_\ell(nq) H_\ell^{(1)}(q)}, \\ b_\ell &= \frac{J_\ell(q) H_\ell^{(1)\prime}(q) - J'_\ell(q) H_\ell^{(1)}(q)}{n J_\ell(nq) H_\ell^{(1)\prime}(q) - J'_\ell(nq) H_n^{(1)}(q)}. \end{aligned} \quad (7)$$

Similar to formulas (1) and (2), we introduced the size parameter $q = k_m a$ and relative refractive index $n = n_p/n_m$. These coefficients are symmetrical: $a_{-\ell} = a_\ell$, $b_{-\ell} = b_\ell$. The extinction, absorption, and scattering cross sections are given by $\sigma_{\text{ext}} = 2aLQ_{\text{ext}}$, $\sigma_{\text{abs}} = 2aLQ_{\text{abs}}$, $\sigma_{\text{sca}} = 2aLQ_{\text{sca}}$, where $2aL$ presents the geometrical cross section (the length of the cylinder $La \gg a$), and related efficiencies Q for TE mode are expressed by coefficient a_ℓ only⁴

$$Q_{\text{ext}} = \frac{2}{q} \sum_{n=-\infty}^{\infty} \text{Re } a_n, \quad Q_{\text{sca}} = \frac{2}{q} \sum_{n=-\infty}^{\infty} |a_n|^2, \quad Q_{\text{abs}} = Q_{\text{ext}} - Q_{\text{sca}}. \quad (8)$$

The time-averaged Poynting vector is given by^{3,21}

$$\langle \mathbf{S} \rangle = \frac{c}{8\pi} \text{Re}(\mathbf{E} \times \mathbf{H}^*), \quad (9)$$

where around the cylinder the fields are given by $\mathbf{E} = \mathbf{E}^{(i)} + \mathbf{E}^{(s)}$, $\mathbf{H} = \mathbf{H}^{(i)} + \mathbf{H}^{(s)}$ while inside the cylinder $\mathbf{E} = \mathbf{E}^{(t)}$ and $\mathbf{H} = \mathbf{H}^{(t)}$. For the discussed case of normal incidence and the TE wave, the z component of the Poynting vector is zero (note that for a case of plane wave with circular polarization $S_z \neq 0$ even for the normal incidence⁸); thus, all field lines lie within the xy plane. The components of the Poynting vector

in polar coordinates are $\langle S \rangle_r$ and $\langle S \rangle_\varphi$. The field lines follow the solution of a differential equation:

$$\frac{dr}{d\varphi} = r \frac{\langle S \rangle_r}{\langle S \rangle_\varphi}. \quad (10)$$

To explain the radiative damping effect let us present the amplitude a_ℓ as $a_\ell = \Re_\ell / (\Re_\ell + i\Im_\ell)$, where \Re_ℓ is used for the numerator of a_ℓ in Eq. (7)

$$\begin{aligned} \Re_\ell &= n J_\ell(nq) J'_\ell(q) - J'_\ell(nq) J_\ell(q), \\ \Im_\ell &= n J_\ell(nq) N'_\ell(q) - J'_\ell(nq) N_\ell(q), \end{aligned} \quad (11)$$

where $N_\ell(q)$ is the Neumann function²² (in some books notation $Y_\ell(z)$ is used for this function).

According to the well-known analytical properties of scattering amplitudes (see, e.g., Refs. 23 and 24), the poles of the amplitude correspond to eigenmodes. Now we have to expand \Re_ℓ and \Im_ℓ functions at small q . Employing the well-known expansion for Bessel functions²²

$$J_\ell(z) = \left(\frac{z}{2}\right)^\ell \sum_{m=0}^{\infty} \frac{\left(-\frac{z^2}{4}\right)^m}{m! \Gamma(\ell+m+1)}, \quad (12)$$

it is easy to obtain the leading term in the numerator of a_ℓ

$$\Re_\ell \approx \begin{cases} \frac{n(n^2-1)}{16} q^3, & \text{for } \ell=0 \\ \frac{n^{\ell-1}(n^2-1)}{2^{2\ell} \ell! (\ell-1)!} q^{2\ell-1}, & \text{if } \ell>0. \end{cases} \quad (13)$$

In contrast to a spherical particle, where the Mie expansion starts with the dipole term $\ell=1$ (see Refs. 3–6), the cylinder also contains the monopole term $\ell=0$. The expansion of \Im_ℓ function at small q contains the product of convergent Bessel functions $J_\ell(q)$ to divergent Neumann functions $N_\ell(q)$. As a result the leading term in this expansion is presented by

$$\Im_\ell \approx \begin{cases} \frac{2n}{\pi q} + \dots, & \text{for } \ell=0 \\ \frac{n^{\ell-1}(n^2+1)}{\pi q} + \dots, & \text{if } \ell>0. \end{cases} \quad (14)$$

We omit the terms proportional to q and its higher powers in (14). Plasmon resonances at $q \rightarrow 0$ correspond to $n(\omega)^2 = -1$ for all modes with $\ell \geq 1$. It is different from the spherical particle where all the modes correspond to different resonant frequencies:^{24,25} $n(\omega_\ell)^2 = -(\ell+1)/\ell$.

Far from plasmon resonance frequencies the inequality $|\Im_\ell| \gg |\Re_\ell|$ holds, thus, $a_\ell \approx -i\Re_\ell/\Im_\ell$, which yields

$$a_0 \approx -i \frac{\pi}{32} (n^2-1) q^4,$$

$$a_\ell \approx -i \frac{\pi}{2^{2\ell} \ell! (\ell-1)!} \frac{n^2-1}{n^2+1} q^{2\ell}, \quad \text{for } \ell>0. \quad (15)$$

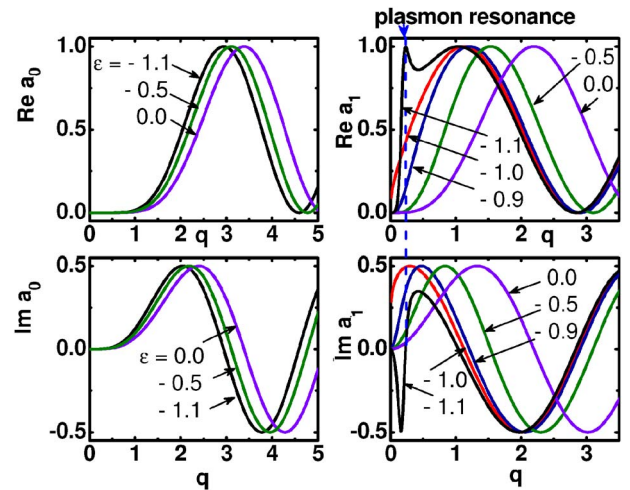


FIG. 1. (Color online) Real and imaginary parts of amplitudes a_ℓ vs size parameter q for $\ell=0$ (monopole) and $\ell=1$ (dipole). Similar behavior can be seen for other amplitudes with $\ell>1$. All amplitudes tend to zero at $q \rightarrow 0$. With dielectric permittivity $-1 < \epsilon < 0$ real part of these amplitudes monotonously increases at small q and reaches the first resonance (similar to Mie resonance in sphere) at q value by the order of unity, e.g., $\text{Re } a_1$ reaches first maximum at $q \approx 2.2$ with $\epsilon=0$ and at $q \approx 1.1$ with $\epsilon=-1$, i.e., move into a smaller q value with a smaller ϵ . Plasmon resonance, related to anomalous light scattering, appears at small q and $\epsilon < -1$ and the position of the resonance moves into larger q values with smaller ϵ . Similar resonances can be seen for all other amplitudes with $\ell>1$.

One can see that the dominant term at small q is presented by dipole radiation with $\ell=1$; thus, $Q_{\text{sca}} \approx 4|a_1|^2/q$ and we arrive to Rayleigh formula (2). However, the exact plasmon resonance corresponds to the situation when $\Im_\ell(n, q)=0$. Thus, a correct description of the resonances requires accounting of \Re_ℓ contribution in the resonant denominators, which results in finite and real values $a_\ell=1$ at the resonant frequencies even in the absence of usual dissipation, i.e., with $\text{Im } \epsilon=0$. For this “nondissipative” case with $-1 < n^2 < 0$ all the amplitudes tend to zero at $q \rightarrow 0$. With a bigger size parameter, these amplitudes demonstrate resonances similar to the Mie resonances of sphere^{24,25} (see in Fig. 1). The plasmon resonances arise at small q and $n^2 < -1$. They arise just for modes with $\ell \geq 1$ and do not arise for the monopole mode $\ell=0$. These resonances for small q are extremely sharp. Trajectories of these resonances follow equation $\Im_\ell(n, q)=0$. To find this equation for small q , it is sufficient to take into account the term proportional q^2 only. As a result, we arrive at the following:

$$\begin{aligned} n^2 + 1 &\approx \frac{q^2}{8} (n^2 - 1) \left[2 + n^2 - 4 \log \frac{qC}{2} \right], \quad \text{for } \ell=1, \\ n^2 + 1 &\approx \frac{q^2}{4} (n^2 - 1) \left[\frac{1}{\ell-1} + \frac{n^2}{\ell+1} \right], \quad \text{for } \ell>1, \end{aligned} \quad (16)$$

where $\log C \equiv \gamma \approx 0.577$ is the Euler’s constant.

The trajectories of the first resonances on the plane of parameters $\{q, n^2\}$ are shown in Fig. 2(a). At small q these trajectories follow Eqs. (17) and tend to limit $n^2=-1$ at q

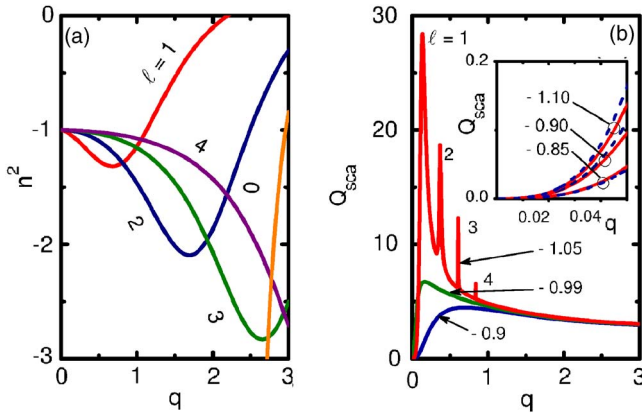


FIG. 2. (Color online) (a) The trajectories of the first resonances ($\ell=0, 1, 2, 3, 4$) found from the equation $I_\ell(n, q)=0$. At $q \approx 0.7$, $\epsilon \approx -1.3$ for dipole the anomalous scattering resonance is converged with the nearest Mie resonance, and ϵ increases further at $q > 0.7$. The trajectories of all other resonances with $\ell > 1$ demonstrate a similar behavior. (b) Normalized scattering cross section vs size parameter q for different values of $\epsilon = n^2 = -0.9, -0.99$, and -1.05 . With $-1 < \epsilon < 0$ scattering demonstrates “normal” Rayleigh-type behavior. With $n^2 < -1$, one can see new multiple resonances, originated by anomalous light scattering. Insert shows that Rayleigh formula (2) near $n^2 \approx -1$ is applicable just for extra small values of q , e.g., $q < 0.03$. The solid curves are calculated according to Rayleigh formula, and the dotted curves according to the exact Mie solution.

$\rightarrow 0$. The amplitudes a_ℓ are equal to one everywhere along the corresponding trajectories. One can see from Fig. 2(a) that at small q resonances arise with $n^2 < -1$. They produce great scattering effect, which can be seen in Fig. 2(b). Although the dipole resonance is dominant, it has nothing in common with the usual Rayleigh scattering. To explain the difference let us use the dielectric permittivity from the approximation of the Drude model

$$\epsilon = \epsilon' + i\epsilon'' = n^2 = 1 - \frac{\omega_p^2}{\omega^2 + \gamma^2} + i\frac{\gamma}{\omega} \frac{\omega_p^2}{\omega^2 + \gamma^2}. \quad (17)$$

Here, as usual ω_p is used for a plasma frequency and γ for collision frequency. Substituting (17) into the Rayleigh formula (2), we arrive at the Lorenzian contour

$$Q_{\text{sca}}^{(\text{Ra})} = \frac{\pi^2}{4} \frac{\omega_{sp}^4}{(\omega^2 - \omega_{sp}^2)^2 + \omega^2 \gamma^2} q^3, \quad (18)$$

where $\omega_{sp} = \omega_p / \sqrt{2}$ is resonance frequency for surface plasmon. In this case the width of the resonance is related to dissipation parameter γ . In a similar way we can write the exact scattering for a dipole mode, $Q_{\text{sca}} \approx 4|a_1|^2/q$, using $a_1 = \mathfrak{R}_1/(\mathfrak{R}_1 + i\mathfrak{I}_1)$, where \mathfrak{R}_1 and \mathfrak{I}_1 are presented by formulas (13) and (14). Using the Drude formula (17) with $\gamma=0$, we once again arrive to Lorenzian contour

$$Q_{\text{sca}}^{(\text{Ra})} = \frac{\pi^2}{4} \frac{\omega_{sp}^4}{(\omega^2 - \omega_{sp}^2)^2 + \frac{\pi^2 q^4 \omega_{sp}^4}{16}} q^3. \quad (19)$$

The width of the resonance, however, is determined by parameter $\gamma_s = \pi\omega_{sp}q^2/4$, which plays the same role as parameter γ in (18). This dissipation is related to plasmon emission, i.e., radiative mechanism of dissipation. It is known that plasmon has a finite lifetime τ_p , which was estimated as $1/\tau_p \approx v_F/a$, where v_F is the Fermi velocity of electrons (see Ref. 26). However, this mechanism is related to collision of electrons with particle surface. Pay attention that lifetime may vary also due to interaction with surrounding interfaces.²⁷ Solution of Maxwell equations yields according to (19) efficient lifetime $1/\tau_p \approx \pi a^2 \omega_{sp}^3 / 4c^2$, which is related to plasmon emission (radiative damping). The charges under approach of classical electrodynamics radiate when they move with acceleration. For example, the dipole rotated in one plane with constant angular velocity Ω produces radiation with intensity $I \propto \Omega^4$.

As all amplitudes a_ℓ at the frequencies ω_ℓ of the appropriate plasma resonances tend to one, we arrive to resonant scattering cross section

$$Q_{\text{ext}} = Q_{\text{sca}} \approx Q_{\text{sca}}^{(\ell)} = \frac{4}{q_\ell} = \frac{4c}{a\omega_\ell}, \quad (20)$$

where ω_ℓ are resonant frequencies according to Eqs. (16) (contribution of nonresonant frequencies is small; thus, their input into the scattering cross section can be neglected). It is clear that Eq. (20) is quite different from Rayleigh formula (2). First, it is finite at exact resonance. Second, it has inverse dependence with respect to frequency. Third, according to Eq. (2) efficiency of scattering is sharply reduced with the reduction of the wire radius. The Eq. (20), however, demonstrates an opposite property. Fourth, the maximal field enhancement at $r=a$, $\varphi=\pi/2$ for the case of Rayleigh scattering is divergent at exact resonance, $|E|_{\text{max}}^2 = |(\epsilon-1)/(\epsilon+1)|^2$. With anomalous scattering, it remains finite at exact resonance, when $\text{Re } \epsilon = -1$ and $\text{Im } \epsilon \rightarrow 0$, $|E|_{\text{max}}^2 = 32/\pi^2 q^4$. Pay attention to the fact that the total scattering cross section at the resonance $\sigma_{\text{sca}}^{(\ell)} = 2aLQ_{\text{sca}}^{(\ell)}$ does not depend on the radius of the wire and, hence, does not vanish at $q \rightarrow 0$. The obtained finite scattering cross section for a wire of zero radius (as well as the infinite field enhancement at $q \rightarrow 0$) obviously is artifact related to the discussed nondissipative limit. In reality dissipation ϵ''_{eff} in Eq. (19) associated with the radiative damping should compete with ϵ'' describing the dissipation in (17). The anomalous scattering may be realized provided at $\epsilon'' \ll \epsilon''_{\text{eff}}$, i.e., if

$$\epsilon'' \ll \frac{\pi q^{2\ell}}{2^{2\ell} \ell! (\ell-1)!!}. \quad (21)$$

It is similar to the condition for spherical particles, found in Refs. 16 and 19. At any fixed value of ϵ'' , the inequality (21) is violated at $q \rightarrow 0$. It means that anomalous scattering can be observed, but not for “too small” particles. Increasing ℓ also results in infringement of an inequality (21). It means that with certain ℓ_{max} , the normal Rayleigh scattering is restored. The restriction (21) explains why the anomalous scattering was not revealed experimentally till now. First, for the majority of the investigated metals, such as gold and silver, the necessary condition $\epsilon''(\omega_\ell) \ll 1$ is not carried out. Second,

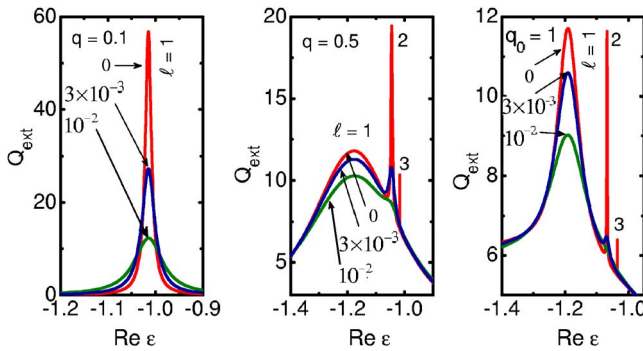


FIG. 3. (Color online) Spectral dependencies of extinction coefficients for different size parameters: $q=0.1$ (a), 0.5 (b), and 1 (c). Three curves in each plot correspond to different values of dissipation parameter $\gamma/\omega_p=0$, 3×10^{-3} and 10^{-2} . For nondissipative material $\gamma=0$ one can clearly see three resonances at $q=0.5$ and 1 .

the anomalous scattering can be observed only for a few first resonances $\ell < \ell_{\max}$. It is illustrated in Fig. 3, where the spectral dependencies of extinction coefficients are shown for dielectric permittivity ϵ according to Drude model (17) with different values of dissipation parameter γ/ω_p . For metals $\omega_p \approx 10^{15}-10^{16} \text{ s}^{-1}$ and $\gamma \approx 3 \times 10^{13}-3 \times 10^{14} \text{ s}^{-1}$, thus, ratio $\gamma/\omega_p > 10^{-2}$ corresponds to highly dissipated media, $\gamma/\omega_p \approx 10^{-2}$ corresponds to “good metals,” and $\gamma/\omega_p \approx 3 \times 10^{-3}$ corresponds to a particular case of weakly dissipated media. From Fig. 3, one can see that the extinction cross section is finite at resonant frequencies even for the nondissipative limit $\gamma=0$. At small q , only the dipole resonance can be detected, while the maximal resonance magnitude is strongly diminished with an increase of the dissipation rate. Even for $\gamma/\omega_p \approx 10^{-2}$, it is by the order of magnitude less than for the nondissipative limit. With a bigger size parameter, very sharp quadrupole and octopole resonances can be seen at the non-dissipative limit. They cannot be seen even for “good metals” because these resonances are strongly suppressed by weak dissipation. However, for some particular case of weakly dissipated media, one can see in some range of size parameter the inverse hierarchy of resonances, when the cross section *increases* with an increase of order of the resonance, i.e., with an increase of ℓ . For example the quadrupole resonance $\ell=2$ may be stronger than the dipole resonance $\ell=1$. Similar inverse hierarchy of resonances was also predicted for spherical nanoparticles.^{16,19}

The possible candidates for manifestation of anomalous scattering with nanowires are the same as suggested for anomalous scattering in nanoparticles:^{16,19} potassium in KCl matrix and aluminium in vacuum. One can see in Fig. 4 the inverse hierarchy of resonances for Al wire in some range of wire radius. Calculations were done according to the exact formulas (7) and (8). Optical properties of Al are taken from Ref. 28. Dependence $\epsilon(\omega)$ for bulk Al is approximated by the Drude formula, where ω_p and γ are regarded ω dependent to fit better with the experimental data.²⁸ In order to take into account collisions of free carriers with the wire surface the effective collision frequency²⁶ $\gamma_{\text{eff}}=\gamma+v_F/a$ is introduced. Here v_F is the Fermi-velocity of electrons; $v_F=10^8 \text{ cm/s}$ for Al.²⁹ With small radius a , one can see only the dipole resonance, similar to Rayleigh scattering. This dipole resonance

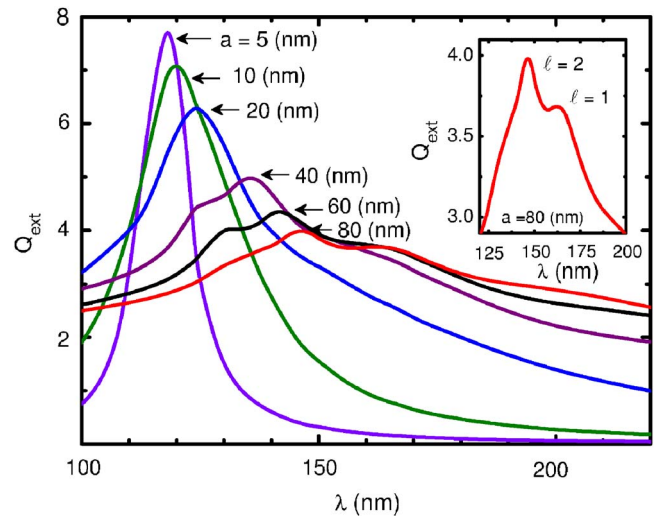


FIG. 4. (Color online) Extinction cross section calculated for Al with different radii of wires. Experimental values of ϵ^{28} were used in calculations.

has a red shift with increase of wire radius. Other resonances are suppressed in full agreement with Eq. (21). However with $a=60 \text{ nm}$, the quadrupole resonance appears and with $a=80 \text{ nm}$, it becomes more intensive than the dipole one. Manifestation of inverse hierarchy is a clear confirmation of anomalous scattering effect. However, one should remember that oxidation of Al strongly suppresses the efficiency of plasmon excitation³⁰ [Al_2O_3 is not transparent below 150 nm (Ref. 28)].

Although far-field effects of anomalous scattering are highly suppressed by dissipation, the most appealing manifestation of the anomalous scattering takes place in the near field where corresponding effects are less sensitive to dissipation rate.

III. ENERGY FLUX AND THE BIFURCATIONS OF THE POYNTING VECTOR FIELD

According to Eqs. (4)–(7), the field distribution depends, in general, on three parameters: size parameter q and real and imaginary parts of dielectric permittivity $\epsilon=n^2=\epsilon''+i\epsilon'$. We start with nondissipative material $\epsilon''=0$, where effects of radiative damping are the most pronounced. According to our previous consideration, plasmon resonances arise at $n^2 \leq -1$. With $n^2 \leq -1$ effects of the anomalous light scattering can be seen in far field; see, e.g. scattering cross section in Figs. 2(b) and 3. With $n^2=-1$ effects of the radiative damping cannot be seen in the far field; however, they produce complex modification of *near-field structure*. The reason for these modifications is the interference of a few different radiative modes, where contribution of different amplitudes a_ℓ varies vs size parameter. It is known that for a small spherical particle this interference produces a field distribution quite different from the dipole scattering.^{18–20} However, we expect that similar modifications of the near field for nanowire should be more complicated than for a sphere. The reason is that the resonant frequencies of different harmonics

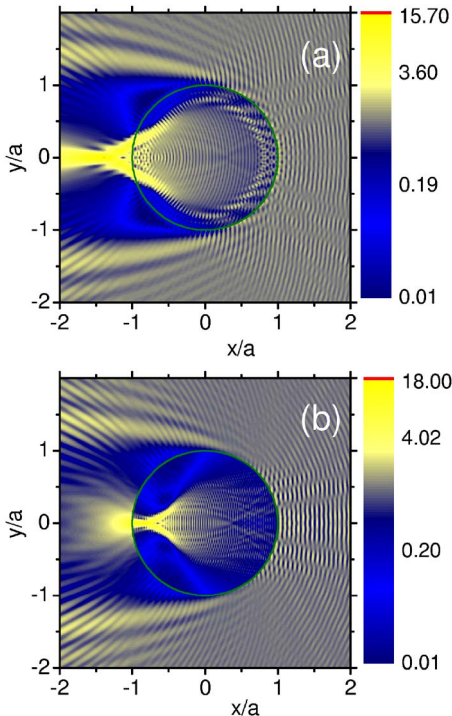


FIG. 5. (Color online) Distribution of intensity $I=|E|^2$ for cylinder with $\epsilon=n^2=2$ (a) and $\epsilon=n^2=4$ (b) with size parameter $q=50$. Under approximation of geometrical optics light is focusing on the output surface of particle when refractive index $n=2$. Calculations were done with $\ell_{\max}=104$. Incident plane wave, where $\mathbf{E} \parallel \mathbf{y}$, comes from $x=\infty$.

with a sphere are well separated, whereas with nanowire they are quite close to each other.

We set the program for calculations according to formulas (4)–(7), using MATHEMATICA software³¹ and checked different test problems. We found the necessary number of terms ℓ_{\max} in sums from the accuracy of boundary conditions fulfillment. Namely, we used the condition

$$\max_{0 \leq \varphi \leq 2\pi} |E_r^{(i)} + E_r^{(s)} - n^2 E_r^{(p)}|^2|_{r=a} \leq \delta. \quad (22)$$

Another condition was related to *structural stability* of the Poynting vector field.¹⁸ It means that the vector field does not change qualitatively with addition of further terms in sums. This stability in our test problems starts with $\delta \approx 10^{-8}$. In our calculations, we set everywhere $\delta \approx 10^{-10}-10^{-11}$. From numerical calculations, a simple relation $\ell_{\max}=[2q]+4$ follows, which is fair for a size parameter $q < 5$. The square brackets mean the integer part. One should mention that the necessary number of terms within the Mie series for spherical particle is given by $\ell_{\max}=[q+4.3q^{1/3}]+1$.³²

We also checked the accuracy of condition $\text{div } \mathbf{S}=0$ within the nondissipative media and limiting values of scattered fields. For $q \ll 1$ and frequencies that are far away from the resonance, our calculations are in agreement with Rayleigh scattering; see inset in Fig. 2(b). We also checked the other limit of big size parameter $q \gg 1$ (limit of geometrical optics) for the case of a transparent particle. It is known

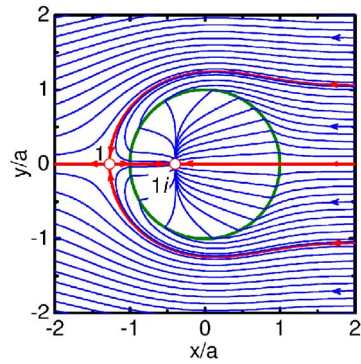


FIG. 6. (Color online) Poynting vector lines for $q=0.1$ and $\epsilon=-1+0.5i$.

that for this case a complex pattern arises, which follows the exact analytical formulas for Kirchhoff integral approximation.^{33,34} For the case of a cylinder this approximation is described by Pearcey integral, which was analyzed in many papers.^{34–36} The complexity of the corresponding pattern is related to interference of a big number of contributing modes and wave caustics. We have made sure that our program produces wave caustics in the correct way. In Fig. 5, an example of the contour plot for distribution of intensity $I=|\mathbf{E}|^2$ is shown for size parameter $q=50$. The Pearcey pattern can be seen well in the pictures. Thus, it is not surprising that case $q \gg 1$ leads to a complicated pattern of the Poynting vector field. Some of these patterns were investigated numerically in Ref. 9.

However for the case of a thin wire with $q \ll 1$, one can expect a simple pattern, which follows dipole scattering. For a case of normal incidence of radiation, the z component of the Poynting vector is identically equal to zero; thus, bifurcations of the Poynting vector field can be investigated on the $\{x,y\}$ plane, following the equation $S_y dx = S_x dy$ [or Eq. (10) in polar coordinates] for the field lines. As mentioned above, when the dissipation rate is not sufficiently small, one can face a situation with Rayleigh scattering. The generic picture for this type of scattering for a small radius with $q=0.1$ and $\epsilon''=0.5$ is presented in Fig. 6. It is quite similar to those for a point dipole, found in the Bohren paper.¹⁷ The phase portrait of the field flow contains a singular point (saddle 1 in Fig. 6), where the separatrixes separate the regions, where field lines either enter the particle or not. Inside the particle there also exists a singular point (node 1*i* in Fig. 6), where energy dissipates. However, as it was shown in Refs. 18–20, this “dipole type” of field structure appears just for a sufficiently big dissipation rate. With a low dissipation rate, the dipole approximation does not hold and the field structure is much more complicated. A similar effect exists for a thin wire.

In Fig. 7, we present a contour plot for the total value of the Poynting vector and corresponding field lines for a small size parameter $q=0.1$ and nondissipative case $\epsilon''=0$. One can see a complicated vector field, which contains eight saddles and eight centers. Two saddles [points 1 and 2 in Fig. 7(a)] are situated very far from the wire at distances of about ten times higher than the wire radius. Another two saddles [points 5 and 6 in Fig. 7(b)] are situated along the axis y

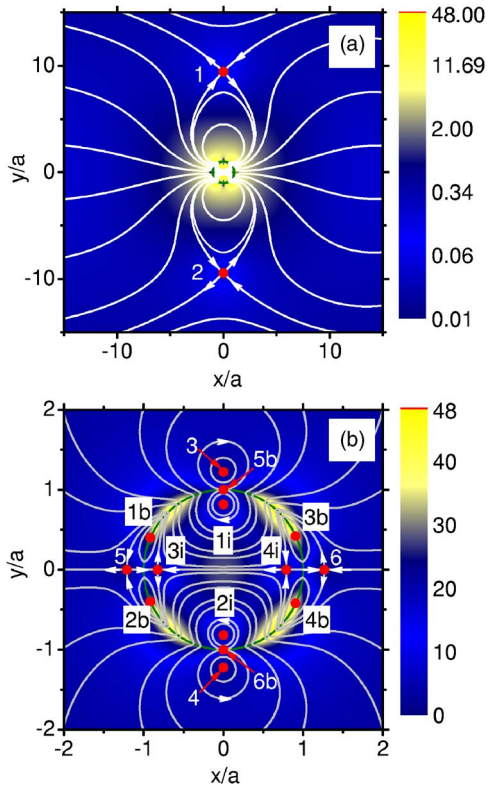


FIG. 7. (Color online) The color in contour plots indicate the absolute value of the Poynting vector $|\mathbf{S}|=\sqrt{S_r^2+S_\varphi^2}$, the white lines show the Poynting vector lines for $q=0.1$ and $\varepsilon=-1+0i$. Upper pictures (a) present the panorama for the “big” distances up to $r\approx 15a$, while the bottom pictures (b) present the details of the Poynting vector inside and outside the particle within the region $r<2a$. Numbers denote different singular points. Six singular points 1–6 are situated outside the particle and four points $1i$ – $4i$ are situated inside the particle. Six other singular points $1b$ – $6b$ are situated on the particle border.

$=0$. In addition, one can see that the scattered field contains two centers (points 3 and 4). Two centers ($1i$ and $2i$) are formed for the flux inside the particle. Two saddle points ($3i$ and $4i$) can also be seen inside the particle. Six singular points: four centers ($1b$, $2b$, $3b$, $4b$) and two saddles $5b$, $6b$ are situated on the particle border. Peculiarities on the border of the particle arise on six points φ_i , where $S_r(a,\varphi_i)=0$. Singular points 1 and 2 arrive from the dipole mode $\ell=\pm 1$. These singular points can be seen in calculations with $\ell_{\max}=1$. Other singular points near the particle surface arrive from the quadrupole mode $\ell=\pm 2$. They can be seen in calculations with $\ell_{\max}=2$. The next modes with $|\ell|>2$ do not produce new singular points, and the Poynting vector picture is stable. However, we have used in the calculations $\ell_{\max}=4$ to provide condition (22) with sufficient accuracy $\delta=1.36\times 10^{-13}$ ($\delta=6.27\times 10^{-10}$ with $\ell_{\max}=3$, but we are doing calculations with $\delta<10^{-10}$ everywhere).

When crossing the particle border, the lines of a Poynting vector are continuous but not necessarily differentiable. The singular points are stable; they do not disappear or change their type with a small variation of q and n^2 parameters. Singularities that are situated on the particle border cannot be

referred to as usual singularities in the theory of non-linear oscillations,³⁷ i.e., they do not correspond to points where both field components $\langle S \rangle_r$ and $\langle S \rangle_\varphi$ tend to zero. The classical theory of oscillations deals with continuous smooth fields. In our case only $\langle S \rangle_r$ value is continuous on the particle border $r=a$, while the $\langle S \rangle_\varphi$ component is discontinuous. Because of continuity of the field lines there is field refraction on the border. It is interesting to note that the angle of the Poynting vector incidence $\theta^{(i)}=\arctan(\langle S \rangle_\varphi/\langle S \rangle_r)|_{r=a+\delta}$ and the angle of refraction $\theta^{(r)}=\arctan(\langle S \rangle_\varphi/\langle S \rangle_r)|_{r=a-\delta}$ for the case $n^2=-1$ are related to a formula, similar to Snell’s law

$$\sin \theta^{(i)}/\sin \theta^{(r)}=-1. \quad (23)$$

Naturally, refraction of the Poynting vector does not follow Snell’s law, in general. It is easy to see at limit $\varphi\rightarrow 0$, which yields $\sin \theta^{(i)}/\sin \theta^{(r)}=n^2$ (for this case $S_\varphi\rightarrow 0$ and ratio of S_r follows continuity of electric induction).

Thus, field lines are refracted into the same directions of normal, similar to ray refraction in the left-handed materials.^{38–40} One can clearly see this type of refraction in Figs. 6 and 7(b).

The existence of singularities of the center point type for nonabsorbing media is evidently permitted by the condition $\text{div } \mathbf{S}=0$. It is clear that the Poynting vector $\mathbf{S}\propto[\mathbf{E}\mathbf{H}]$ is perpendicular to both electric and magnetic fields. Let us consider polarization with a fixed z direction of the magnetic field. In this case polarization of the electric field in $\{x,y\}$ plane is perpendicular to Poynting vector lines. Thus, around the centers one has radially polarized light. Radially polarized light is quite an interesting physical object, which has been analyzed recently in Refs. 41 and 42. Radially polarized light can be focused to a spot size significantly smaller than that for linear polarization; it can be used for particle trapping, etc. There are a few known methods to generate radially polarized light in the vicinity of near-field aperture, either with the help of Mach-Zender interferometer or with the use of mode-forming holographic and birefringent elements (see Ref. 42 and the references therein). Scattering of light

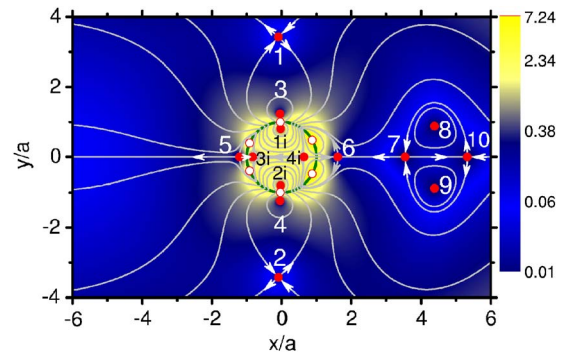


FIG. 8. (Color online) Contour plot of $|\mathbf{S}|=\sqrt{S_r^2+S_\varphi^2}$ and Poynting vector lines for $q=0.35$ and $\varepsilon=-1$. Singular points 1–6 (out of particle), $1i$ – $4i$ (inside the particle) and $1b$ – $6b$ situated on the particle border (numbers are not shown) are of the same type as in Fig. 7. New singular points 7–10 present two saddles (7 and 10) and two centers (points 8 and 9).

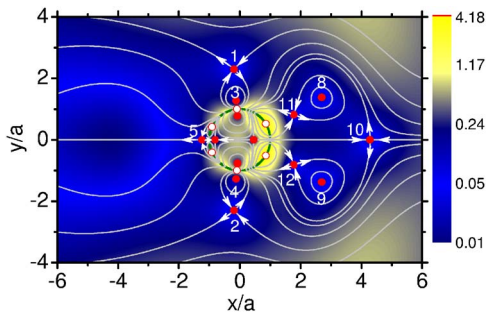


FIG. 9. (Color online) Contour plot of $|S| = \sqrt{S_r^2 + S_\varphi^2}$ and Poynting vector lines for $q=0.6$ and $\epsilon=-1$. Singular points 1–5 and 8–12 (out of particle), 1*i*–4*i* (inside the particle) and 1*b*–6*b* situated on the particle border (numbers are not shown) are of the same type as in Figs. 7 and 8. Two new saddles 11 and 12 appear after collapse of saddles 6 and 7 in Fig. 8.

on a cylinder with surface plasmon resonance presents a new method for the generation of radially polarized light in the nanoscale region.

An increase in the size parameter yields a complication in the phase portrait; a new saddle and center points arise. An example of the phase portrait for $\epsilon''=0$ and the size parameters $q=0.35$, 0.6 , and 1 are shown in Figs. 8–10. One can see modifications in the phase portrait vs size parameter.

It is clear that additional singularities arise due to bifurcations of the Poynting vector field. To analyze these bifurcations, we follow the standard methods of the theory of oscillations.³⁷ We shall start with the nondissipative case, which yields the most numerous transformations of the Poynting vector field. In Fig. 11, we present the trajectories of the singular points that are solutions of

$$\langle S(r, \varphi) \rangle_r = 0, \quad \langle S(r, \varphi) \rangle_\varphi = 0. \quad (24)$$

The positions of these points (and the number of points) depend on size parameter q . This bifurcation diagram in Fig. 11 shows that with $0.1 < q < 1.7$ there are five regions where the phase portraits are qualitatively different. The phase por-

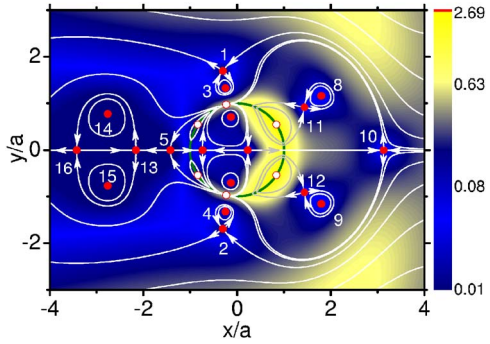


FIG. 10. (Color online) Contour plot of $|S| = \sqrt{S_r^2 + S_\varphi^2}$ and Poynting vector lines for $q=1$ and $\epsilon=-1$. Singular points 1–5 and 8–12 (out of particle), 1*i*–4*i* (inside the particle) and 1*b*–6*b* situated on the particle border (numbers are not shown) are of the same type as in Figs. 8 and 9. Four new singular points 13–16 appear in the shadow region.

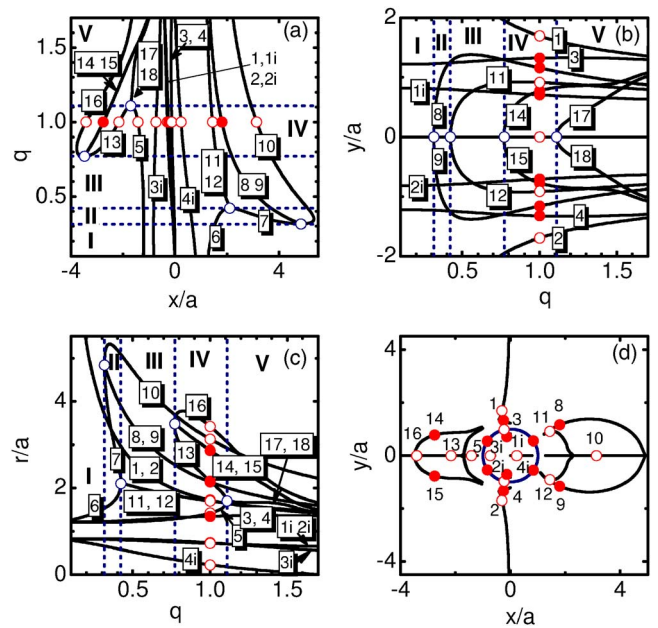


FIG. 11. (Color online) Trajectories of singular points vs size parameter q : $x/a = f_x(q)$ (a); $y/a = f_y(q)$ (b); $r/a = f_r(q)$ (c). Parametric plot (d) presents the trajectories of singular points with variation of the size parameter. Circles with numbers indicate positions of singular points at $q=1$ (see in Fig. 10).

trait within region I is similar to that shown in Fig. 7 and within regions II–IV in Figs. 8–10.

Now we can discuss the scenario of bifurcations vs size parameter, which is illustrated by the bifurcations sequence, presented in Fig. 12. With a small size parameter $q < 0.315$ (region I) the phase portrait for a scattered field $r > a$ contains two saddles on axis $y=0$: one from the side of input radiation ($x > 0$) and the second from the opposite side ($x < 0$). These points numbered 5 and 6 in Fig. 7(b) also exist when the size parameter crosses the first bifurcation value $q=0.315$. However with a bit higher value of q from the side of input radiation ($x/a=4.837$), four singular points (7–10) simultaneously appear; see Fig. 8. Two saddles (points 7 and

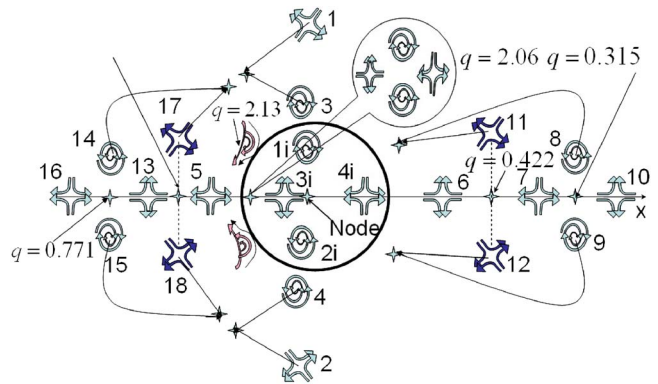


FIG. 12. (Color online) A panorama of bifurcation sequence versus size parameter q . We use special icons to designate singular points and bifurcations: e.g., icon \oplus indicates the saddle points, \odot is used for center (or focus in dissipative media), icon \star means bifurcation point.

10) move along axis $y=0$ in different directions. Another two singular points 8 and 9 are two centers, which move initially in two perpendicular directions. This bifurcation is quite unusual: four singular points within the phase portrait appear from “nothing.” When the size parameter is diminished these four points approach each other and then collapse and vanish at $q=0.315$. It is well known from the catastrophe theory⁴³ that for a generic one-parameter family such a bifurcation is considered to be “nontypical,” i.e., a small perturbation should transform it into a sequence of bifurcations with the appearance of two singular points. However, in the discussed problem the “typical” bifurcation is forbidden by symmetry. As we consider nonabsorbing media (vacuum), the general condition $\text{div } \mathbf{S}=0$ coexists with the singular points of the center and saddle types only. On the other hand, the total Poincaré index should not change during bifurcation, which means that just an equal number of saddles and centers can appear (or vanish) during bifurcation. At the same time, the problem has symmetry in y direction, which plays the role of a selection rule. It is clear that the saddle and the center situated on $y=0$ axis do not fulfill the symmetry condition; while the Poynting vector around the center is directed from left to right in the upper half plane, it is clearly directed from right to left in the bottom half plane. Thus, the first “typical” bifurcation in our case is related to the appearance (or vanishing) of two saddles and two centers. This bifurcation is stable even when one considers a weakly absorbing media; the only change is that the centers are transformed to stable focuses. We are using an icon for the focuses within Fig. 12 to show the effect of weak dissipation (without the dissipation all corresponding points are centers).

The second bifurcation arises at $q=0.422$. When the size parameter changes from 0.315 to 0.422 saddles 6 and 7 move toward each other, they collapse at the bifurcation point and convert into other two saddles (11 and 12 in Fig. 9). These new saddles leave axis $y=0$ and move initially in two perpendicular directions. After this bifurcation just one saddle point 10 remains on the axis $y=0$ at $x>a$.

The third bifurcation at $q=0.771$ repeats the scenario with the creation of four new singular points in the “shadow region” (13–16 in Fig. 10) at $x/a=-2.912$. Saddles 13 and 5 move toward each other and collapse at $q=1.1$ (fourth bifurcation). Two new saddles (17 and 18 in Fig. 11) move initially in two perpendicular directions.

Thus, we have a typical bifurcation with the creation of two saddles and two centers, after which the two saddles convert to two other saddles. It leads to modification of the phase portrait (compare Figs. 9 and 10). These bifurcations first occur from the side of input radiation ($x>0$) and later from the opposite “shadow side” ($x<0$). Similar transformations appear inside the particle: at $q=2.06$ four singular points are created and at $q=2.105$ a bifurcation of two saddles into two other saddles arises.

We wrote the numbers of corresponding points along the trajectories in Fig. 11. We do not show further bifurcations with $q>1.7$ in Fig. 11 because of the strong overlapping of curves. We just note that bifurcations with a collapse of singular points are also possible. For example, eight points collapsed at $q=1.93$.

Dissipation also leads to modifications in the phase portrait. In Fig. 13, we show how the left branch of S-shaped

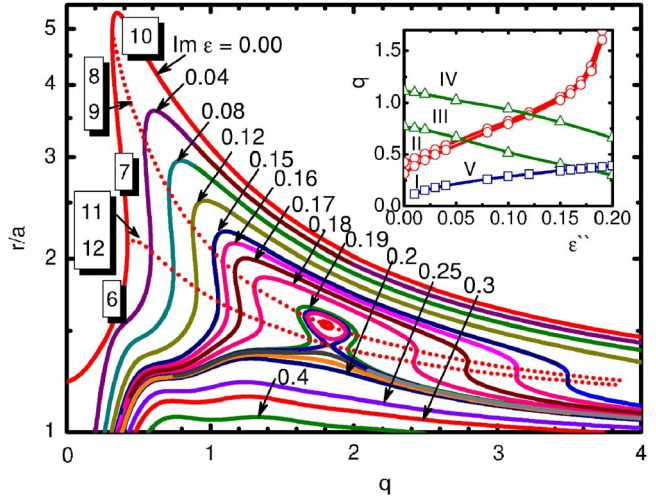


FIG. 13. (Color online) Trajectories of the first singular points versus size parameter q for $\text{Re } \epsilon=-1$ and different dissipation factor ϵ'' . Numbers in the figure denote singular points of the same type as in Fig. 11(c). The dashed lines indicate the trajectories of bifurcation points with vertical derivation $dr/dq=\infty$. These trajectories coincide with the trajectories of the singular points 8, 9 and 11, 12 near bifurcation points. The insertion shows trajectories I and II of corresponding bifurcation points on the plane of q and ϵ'' parameters. Trajectories III-V for other bifurcation points are explained within the text. These five trajectories separate the region shown in the figure into 11 subregions with different types of the Poynting vector field.

solution with singular points 6–12 in Fig. 11 modifies vs the dissipation parameter. It illustrates the motion of corresponding bifurcation points on the plane of parameters q, ϵ'' (see lines I and II in inset). Lines III and IV present the trajectories of bifurcation points of the second (right) S-shaped solution with singular points 3–5 and 13–16 in Fig. 11. The third line V shows the trajectory of a particular point, where a corresponding solution enters into the particle. Each area on the phase diagram (see inset in Fig. 13) corresponds to a new type of phase portrait of the Poynting vector field. Thus, numerous modifications of the Poynting vector field exist with variation of size parameter and dissipation.

We do not show in Fig. 13 bifurcations related to the motion of internal points within the particle. However, these bifurcations also play an important role. We shall demonstrate for a particular case of a small particle with $q=0.1$. As we have mentioned above the Rayleigh scattering should be restored with increase of dissipation. Thus, the picture in Fig. 7(b) should be transformed into Fig. 6. This transformation is quite complicated and it arises after a sequence of bifurcations shown in Fig. 14. The “initial points,” which correspond to $\epsilon''=0$ are presented in the figure as well as their trajectories with variation of ϵ'' . Fourteen singular points (from all the 16 singular points shown in Fig. 7) disappear during this transition from anomalous scattering to Rayleigh scattering. First, points 5, 3*i*, 1*b*, and 6*b* disappear at $\epsilon''=3.6 \times 10^{-3}$. These points move toward each other and finally merge and disappear. The same happens with points 6, 4*i*, 3*b*, and 4*b*; they merge and disappear at $\epsilon''=6.7 \times 10^{-3}$. Points 3 and 5*b* (as well as the symmetrical points 4 and 6*b*)

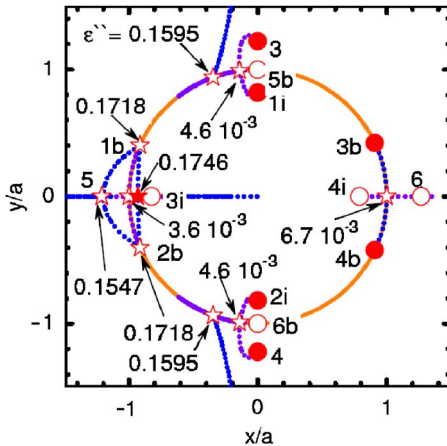


FIG. 14. (Color online) Trajectories of the singular points (dotted lines) with variation of dissipation parameter $\varepsilon'' = \text{Im } \varepsilon$ for the wire with $q=0.1$ and $\text{Re } \varepsilon=-1$. Circular points indicate “initial positions” of singular point at $\varepsilon''=0$ (see in Fig. 7). Star symbols indicate the bifurcation points (corresponding ε'' values are written in the figure).

merge at $\varepsilon''=4.6 \times 10^{-3}$. However, points $1i$ and $2i$ do not disappear. With $\varepsilon''>0$, they transfer from the centers to the foci and move toward the particle border, which they reach at $\varepsilon''=4.9 \times 10^{-3}$. These foci move along the surface into the direction of the “shadow part” of the particle with further increase of ε'' value. Thus, at $\varepsilon''=10^{-2}$ only four singular points remain in the phase portrait: two saddles 1 and 2 , which move close to the particle (these points reach the particle border at $\varepsilon''=0.1595$) and two foci $1i$ and $2i$, which produce two “optical whirlpools” (the term was suggested by Bashevov *et al.*²⁰); see in Fig. 15(a). These foci become smaller with an increase of dissipation and disappear at the moment when two saddles 1 and 2 reach the particle border.

At $\varepsilon''=0.1547$, a new bifurcation occurs; four singular points appear at the point $x/a \approx -1.2$. The phase portrait of Poynting vector lines for $\varepsilon''=0.16$ is shown in Fig. 15(b). It contains only four singular points. Two saddles $1a$ and $2a$ move in different directions along axis $y=0$ and two centers $3a$ and $4a$ move initially in perpendicular directions. Saddle $2a$ reaches the particle border $\varepsilon''=0.1574$ and then continues to move inside the particle along axis $y=0$. Two centers $3a$ and $4a$ reach the particle surface at $\varepsilon''=0.1718$ as it is shown in Fig. 14.

At $\varepsilon''>0.1718$ two “former centers” $3a$ and $4a$ crossed the particle border. During this crossing, they “converted” from centers to nodes. One should remember that this “change in stability” is not a real bifurcation but some kind of “relay race.” In reality, Poynting vector lines inside and outside the wire are described by different equations. These equations have different singular points, the trajectories of which can be expanded formally to the whole space. The Poincaré index is conserved during bifurcations for each given set of equations. However at $\varepsilon''=0.1718$, the trajectory with nodes (inside the wire) crosses the trajectory of saddles (outside the wire). This crossing occurs on the particle border. Thus, at $\varepsilon''>0.1718$, we can see still four singular points as it is shown in Fig. 15(c) for $\varepsilon''=0.173$. We used in Fig.

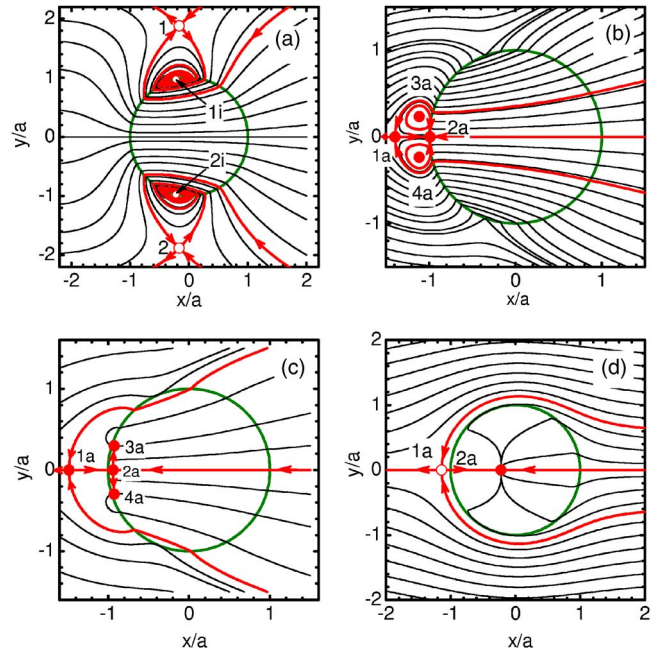


FIG. 15. (Color online) Poynting vector lines for a wire with $q=0.1$ and $\text{Re } \varepsilon=-1$ for different dissipation rates: $\varepsilon''=0.01$ (a), 0.16 (b), 0.173 (c), and 1 (d). The thick lines in present the separatrices of the vector field. On the phase portrait (a) one can see two saddles (points 1 and 2 outside the particle) and two stable focuses (“optical whirlpools,” points $1i$ and $2i$), situated on the particle border. On the phase portrait (d) there is a single saddle (point $1a$ outside the particle) and a single node (point $2a$) inside the particle.

15(c) the same notations $2a$, $3a$, and $4a$ [as in Fig. 15(b)] for the new singular points that arise due to “relay transition.”

The final transformation of the Poynting vector field with a further increase of $\varepsilon''>0.1718$ arise at $\varepsilon''=0.1746$. Two nodes and saddle move toward each other, and at $\varepsilon''=0.1746$ we have bifurcation, which results in the creation of a single node. At $\varepsilon''>0.1746$, the typical Rayleigh scattering picture is restored; see Fig. 15(d). The node inside the particle after this bifurcation continues to move along the axis $y=0$ into the direction of the center (it reaches the center of the wire at the limit $\varepsilon'' \rightarrow \infty$). One can see that the Poynting vector field shown in Fig. 15(d) is of the same type as in Fig. 6.

Similar numerous modifications of the Poynting vector field exist with variation of size parameter and dissipation. A brief overview of these modifications is presented in Fig. 16 as a set of the contour plots of the module of the Poynting vector vs q and ε'' parameters. The “dipole” type of the phase portrait appears just for the case of sufficiently big dissipation.

Additionally, we analyzed the stability of the Poynting vector pattern with respect to the radiation incidence angle. For this case, general formulas (Ref. 6) were used. The results show that all the patterns in Figs. 3–6 are stable. Generally, with a further increase of the radiation incidence angle the Poynting flux pattern becomes simpler. However, we can

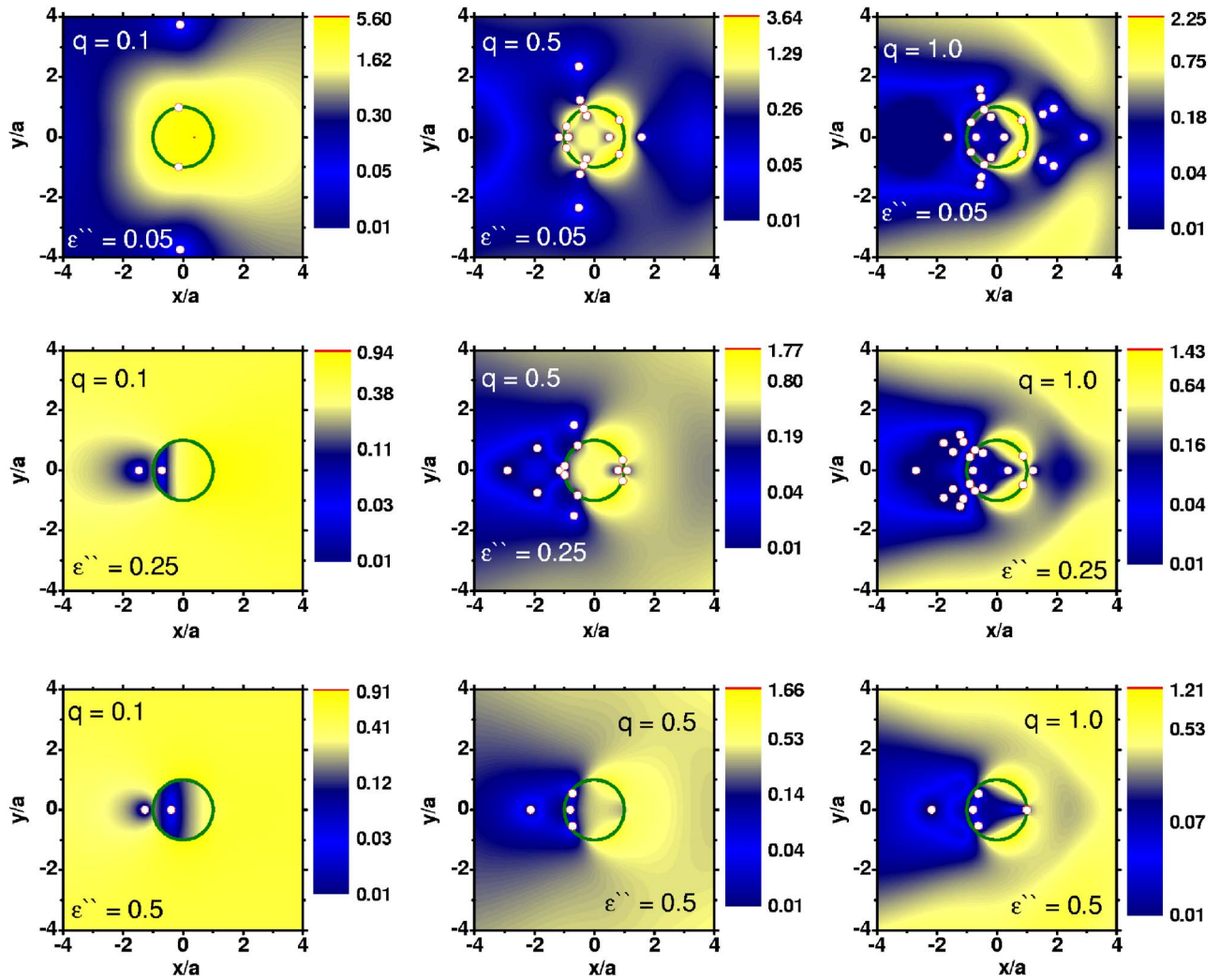


FIG. 16. (Color online) The gray color in contour plots indicate the absolute value of the Poynting vector $|S|$ for the particle with $\epsilon' = \text{Re } \epsilon = -1$. Each column corresponds to fixed size parameter $q = 0.1, 0.5$, or 1.0 . Each row corresponds to fixed dissipation parameter $\epsilon'' = \text{Im } \epsilon = 0.05, 0.25$, or 0.5 . Positions of the singular points are shown by small circles, e.g., the panel with $q = 1$ and $\epsilon'' = 0.05$ contains 20 singular points: ten points out the particle, four points inside the particle, and six points on the particle border.

expect some different effects in angular dependence for the case of nanotubes or for the case of cylindrical waveguide geometry.^{30,44} In the latest case, cylindrical geometry promotes radiative interaction with slow surface excitations.³⁰

The efficiency of scattering evidently increases for smaller size parameters and smaller dissipation. As mentioned above, the theoretical limit at exact resonance, when $\text{Re } \epsilon = -1$ and $\text{Im } \epsilon \rightarrow 0$, yields $|E|_{\max}^2 = 32/\pi^2 q^4$. It means that for the case of nanowire with ratio $\lambda/a = 100$ corresponding $|E|_{\max}^2 \approx 2 \times 10^5$. Thus, this effect may play an important role in surface enhanced Raman scattering (SERS) near single nanowire or nanoparticle. Up to now big values of SERS enhancement $\propto |E|_{\max}^4$, which reach of $>10^{10}$ in some experiments,⁴⁵ were explained by distinct electromagnetic coupling between the localized surface plasmons in aggregates of nanoparticles,^{45–49} in multilayered metal core-shell nanostructures,⁵⁰ or by effects near the edge of nanowire with non-elliptical (e.g., triangular) shape.⁵¹

IV. CONCLUSION

The analysis presented in this paper refers to light scattering by small wires with weak dissipation near plasmon resonant frequencies. The paradigm of simple “dipole type scattering” of objects the size of which is small compared to radiation wavelength exists since the time of Rayleigh and Debye. This paradigm is based on the calculation of the object polarizability in a constant and uniform electric field (see Chap. 92 in Ref. 21). However, this approach ignores the fields that arise due to plasmon emission near plasmon resonance frequencies. Near these frequencies, the scattering problem cannot be analyzed in the dipole approximation. It was demonstrated previously for a spherical particle;^{16,18–20,52} now we extend a similar effect to nanowires. A structure of the Poynting vector in the near field area is obtained. It is shown that small variations of the size parameter and/or the incident light frequency may lead to drastic transformations of the field distribution. Although the

majority of these reconstructions takes place for weakly dissipative materials, some of them still exist even for a relatively big dissipation, e.g., $\epsilon'' > 0.2$; see inset in Fig. 13. Such weakly dissipative materials exist (e.g., aluminium) or they can be created artificially.⁵³

Manipulation in the field structure can be used for different applications in nano optics. For example, the areas with radially polarized light in nanoscale region have a potential interest for applications. In conclusion, we would like to say that numerous modifications in the Poynting vector field are quite general for weakly dissipating materials. Only with a

sufficiently big dissipation one arrives at the “classical” dipole type of scattering.

ACKNOWLEDGMENTS

We are very thankful to S. I. Anisimov, M. I. Tribelsky, N. Arnold, and Z. B. Wang for critical comments and discussions. This work was (in part) supported by the Russian Basic Foundation for Research (Grants No. 04-02-17225 and No. 04-02-16972).

*Corresponding author.

Electronic address: Boris_L@dsi.a-star.edu.sg

¹Lord Rayleigh, Philos. Mag. **36**, 165 (1918).

²M. Kerker (Ed), Proc. SPIE **951**, Part 2, 495-586 (1988).

³J. A. Stratton, *Electromagnetic Theory* (McGraw-Hill, New York, 1941).

⁴H. C. van de Hulst, *Light Scattering by Small Particles* (Dover, New York, 2000).

⁵M. Kerker, *The Scattering of the Light and Other Electromagnetic Radiation* (Academic Press, New York, 1969).

⁶C. F. Bohren and D. R. Huffman, *Absorption and Scattering of Light by Small Particles* (Wiley, New York, 1983).

⁷M. Yamada, M. Saitoh and H. Ooki, Appl. Phys. Lett. **69**, 3659 (1996).

⁸M. Sato and S. Tokumaru, Electron. Commun. Jpn., Part 2: Electron. **82**, 31 (1999).

⁹W. Zakowich, Phys. Rev. E **64**, 066610 (2001).

¹⁰R. Ruppin, Opt. Commun. **211**, 335 (2002).

¹¹D. Li and Y. N. Xia, Nat. Mater. **3**, 753 (2004).

¹²W. Srituravanich, N. Fang, C. Sun, Q. Luo, and X. Zhang, Nano Lett. **4**, 1085 (2004).

¹³U. Schröter and A. Dereux, Phys. Rev. B **64**, 125420 (2001).

¹⁴A. Ambrosio, B. Piccirillo, A. Sasso, and E. Santamato, Opt. Commun. **230**, 337 (2004).

¹⁵B. Z. Tian, X. Y. Liu, L. A. Solovyov, Z. Liu, H. F. Yang, Z. D. Zhang, S. H. Xie, F. Q. Zhang, B. Tu, C. Z. Yu, O. Terasaki, and D. Y. Zhao, J. Am. Chem. Soc. **126**, 865 (2004).

¹⁶M. I. Tribelsky, Sov. Phys. JETP **59**, 534 (1984).

¹⁷C. F. Bohren, Am. J. Phys. **51**, 323 (1983).

¹⁸Z. B. Wang, B. S. Luk'yanchuk, M. H. Hong, Y. Lin and T. C. Chong, Phys. Rev. B **70**, 035418 (2004).

¹⁹B. S. Luk'yanchuk and M. I. Tribelsky, *Anomalous Light Scattering by Small Particles and Inverse Hierarchy of Optical Resonances* (St. Petersburg Union of the Scientists, St. Petersburg, Russia, 2005), pp. 101–117.

²⁰M. V. Bashevov, V. A. Fedotov, and N. I. Zheludev, Opt. Express **13**, 8372 (2005).

²¹L. D. Landau and E. M. Lifshitz, *Electrodynamics of Continuous Media* (Pergamon Press, New York, 1994).

²²E. Jahnke, F. Emde, and F. Lösch, *Tables of Higher Functions*, 6th ed. (McGraw-Hill, New York, 1960).

²³L. D. Landau and E. M. Lifshitz, *The Quantum Mechanics (Non-Relativistic Theory)*, 3rd ed. (Butterworth-Heinemann, Oxford, 1999), Chap. 128.

²⁴M. H. Fields, J. Popp, and R. K. Chang, In *Progress in Optics*,

edited by E. Wolf (Elsevier, New York, 2000), vol. 41.

²⁵M. Born and E. Wolf, *Principles of Optics*, 7th ed. (Cambridge University Press, Cambridge, England, 1999).

²⁶U. Kreibig and M. Vollmer, *Optical Properties of Metal Clusters* (Springer-Verlag, Berlin, 1995).

²⁷R. Ruppin and O. J. F. Martin, J. Chem. Phys. **121**, 11358 (2004).

²⁸E. D. Palik, *Handbook of Optical Constants of Solids* (Academic Press, Orlando, 1985–1998).

²⁹T. Wegehaupt and R. E. Doezeema, Phys. Rev. B **16**, 2515 (1977).

³⁰C. Mizumski, Phys. Lett. **40A**, 187 (1972).

³¹S. Wolfram, *Mathematica*, 4th ed. (Wolfram Media and Cambridge University Press, Cambridge, England, 1999).

³²P. W. Barber and S. C. Hill, *Light Scattering by Particles: Computational Methods* (World Scientific, Singapore, 1990).

³³J. J. Stamnes, *Waves in Focal Regions* (Adam Hilger, Bristol, 1986).

³⁴J. N. Connor and D. Farrelly, J. Chem. Phys. **75**, 2831 (1981).

³⁵J. N. Connor and P. R. Curtis, J. Math. Phys. **25**, 2895 (1984).

³⁶J. F. Nye, J. Opt. A, Pure Appl. Opt. **5**, 495 (2003).

³⁷A. A. Andronov, A. A. Vitt, and S. E. Khaikin, *Theory of Oscillations* (Pergamon, London, 1966).

³⁸V. Veselago, Sov. Phys. Usp. **10**, 509 (1968).

³⁹R. A. Shelby, D. R. Smith, and S. Shultz, Science **292**, 77 (2001).

⁴⁰J. B. Pendry, Phys. Rev. Lett. **85**, 3966 (2000).

⁴¹C. C. Sun and C.-K. Liu, Opt. Lett. **28**, 99 (2003).

⁴²R. Dorn, S. Quabis, and G. Leuchs, Phys. Rev. Lett. **91**, 233901 (2003).

⁴³V. I. Arnold, *Catastrophe Theory* (Springer-Verlag, Berlin, 1992).

⁴⁴V. S. Gurevich and M. N. Libenson, Ultramicroscopy **57**, 277 (1995).

⁴⁵M. Futamata, Y. Maruyama, M. Ishikawa, J. Phys. Chem. **108**, 13119 (2004).

⁴⁶M. Quinten, Appl. Phys. B: Lasers Opt. **73**, 245 (2001).

⁴⁷J. P. Kottnmann and O. J. F. Martin, Opt. Express **8**, 33954 (2001).

⁴⁸V. S. Zuev, G. Y. Zueva, A. V. Fransson, Opt. Spectrosc. **95**, 368 (2003).

⁴⁹K. Li, M. I. Stockman, D. J. Bergman, Phys. Rev. Lett. **91**, 227402 (2003).

⁵⁰H. X. Xu, Phys. Rev. B **72**, 073405 (2005).

⁵¹J. P. Kottnmann, O. J. F. Martin, D. R. Smith, and S. Shultz, Chem. Phys. Lett. **341**, 1 (2001).

⁵²A. B. Evlyukhin and S. I. Bozhevolnyi, JETP Lett. **81**, 218 (2005).

⁵³M. Scheffler, M. Dressel, M. Jourdan, and H. Adrian, Nature (London) **438**, 1135 (2005).